Supplementary information

Temperature dependence of near-field radiative heat transfer above room temperature

C. Lucchesi[1,2]*, R. Vaillon[2,1], P.-O. Chapuis[1]

[1] Univ Lyon, CNRS, INSA-Lyon, Université Claude Bernard Lyon 1, CETHIL UMR5008, F-69621, Villeurbanne, France
[2] IES, Univ Montpellier, CNRS, Montpellier, France

christophe.lucchesi@insa-lyon.fr

A.1. Predictions of thermal radiative conductances

An analysis similar to that of Fig. 2 is performed with a spherical emitter instead of a planar one facing a planar substrate. The Proximity Approximation (Derjaguin) is applied for the evanescent waves. In Fig. A.1a, the total conductance as a function of emitter temperature is almost independent of distance because of the small contribution of evanescent waves caused by the curved geometry of the emitter. In fact, the curvature of the surface of the sphere leads to a variable distance gap with the surface of the sample, ranging from d at the closest and up to $d + R$ at the largest, R being the radius of the sphere. For a sphere having a radius of the order of a few tens of micrometers (20 µm in Fig. A.1a,b), a major part of the sphere surface is too far from that of the planar material to allow evanescent waves to contribute significantly to radiative heat transfer. At the largest distance, both the plane-plane and sphere plane geometry tend to the same total radiative conductance (compare Fig 1a of the main paper and Fig A.1a) because the effect of the curvature of the sphere becomes negligible. Another effect of the curvature of the sphere is a flattening of the exponent for the different contributions in the near field while similar exponents are found in the far field compared with a planar emitter (Fig A.1b).

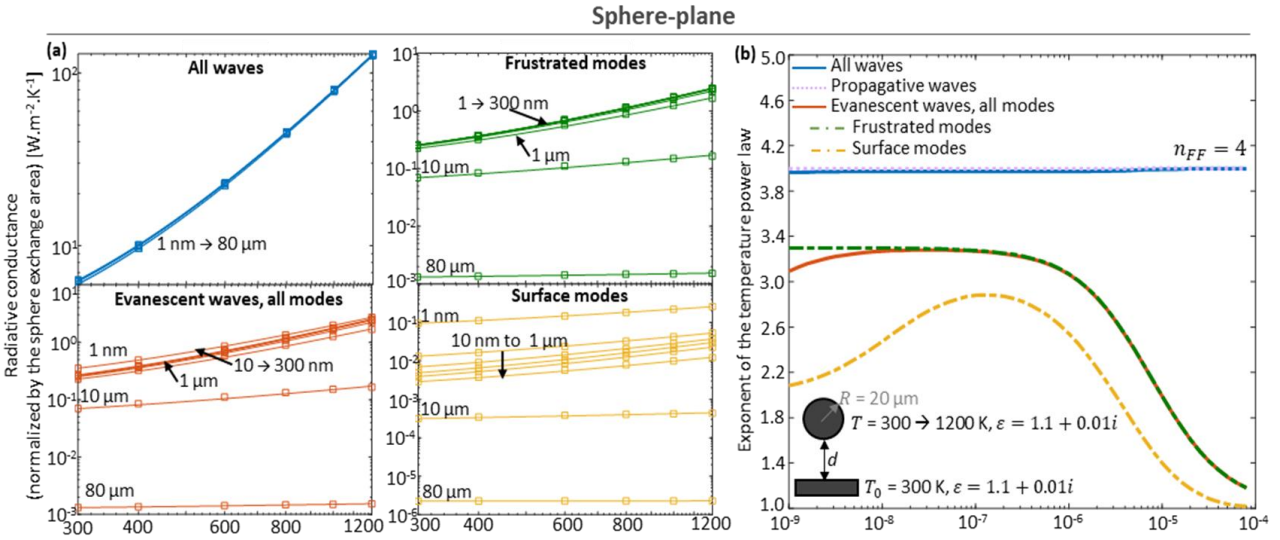

Fig. A.1: Determining the temperature power law of the radiative conductance between a sphere and a plane. (**a**) Numerical calculations (squares) of the radiative thermal conductance for the media having both a dielectric function $\boldsymbol{\varepsilon}$ = 1.1+0.01i. Numerical results are fitted by the analytical expression (Eq. 3**Erreur ! Source du renvoi introuvable.** in the manuscript) of the radiative conductance (lines). (**b**) Exponent of the temperature power law as a function of distance between materials considering the total radiative heat flux (blue, solid), the propagative wave contribution (light purple, dot), the evanescent wave contribution (red, solid) with the frustrated (green, dash-dot) and surface modes (yellow, dash-dot).

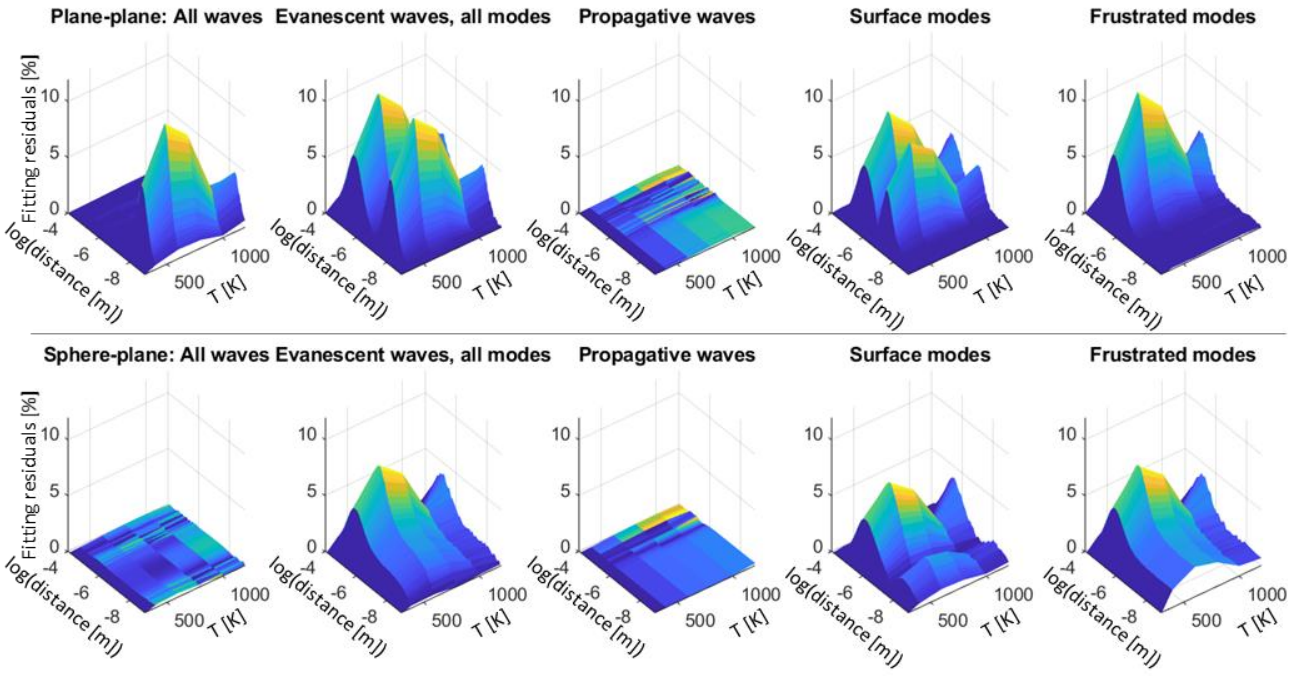

Fig. A.2: Relative residuals (fitting deviations) of the fits of the numerical calculations by the analytical temperature power law (Eq. 3) as a function of distance (logarithmic scale) and emitter temperature. Residuals are shown for each wave contributions and for both the plane-plane (top) and the sphere-plane (bottom) configurations.

Fig. A.2 shows 2D-plots representing the relative residuals of the fit of the fluxes from numerical calculations (fluctuational electrodynamics) by the analytical power law (Eq. 3) as a function of distance and emitter temperature, expressed as:

$$residuals(d,T)[\%] = 100 \times \frac{\left|q_{numerical}(d,T) - q_{fit,analytical}(d,T)\right|}{q_{numerical}(d,T)}. \qquad \text{(A.1)}$$

It appears that the fits are very good because relative residuals are never higher than 10 % of the numerical calculations.

A.2. Near-field radiative heat transfer measurements

We provide here all the data of the near-field radiative heat transfer measurements.

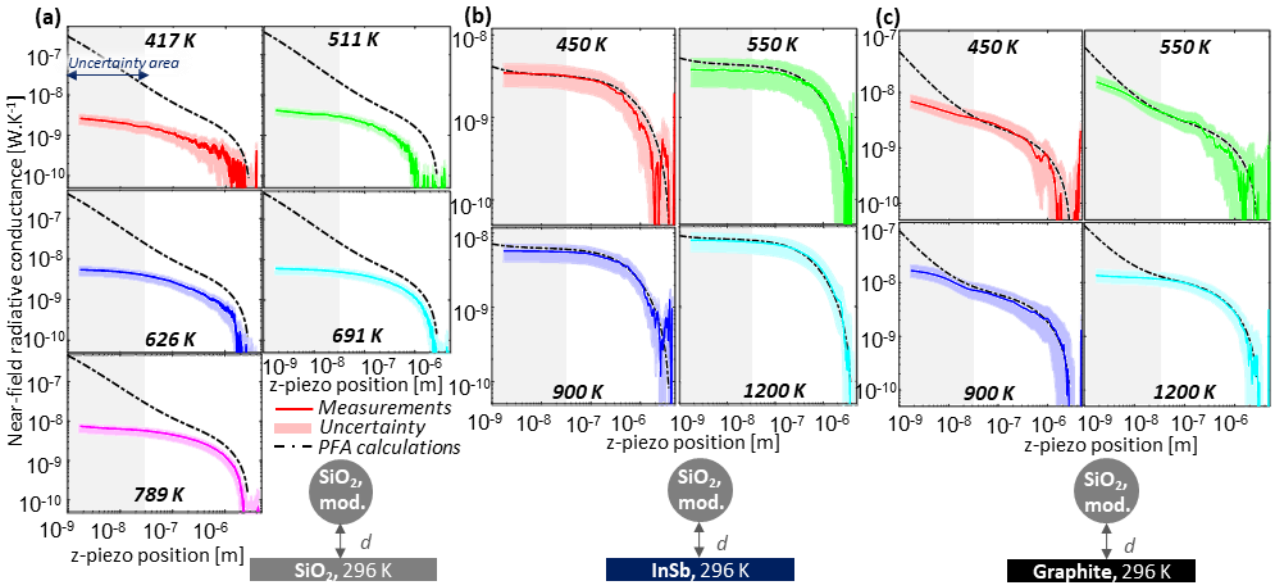

Fig. A.3: Near-field radiative conductance measurements with a modified SiO_2 emitter. Near-field radiative conductance between a modified SiO_2 sphere heated from 417 to 1200 K and a planar substrate at room temperature made of either SiO_2 (**a**), InSb (**b**) or graphite (**c**), as a function of z-piezo position. The grey-shaded area represents the range where there are large distance determination uncertainties induced by the roughness of the materials and mechanical vibrations (see Fig. A.6).

In all configurations a good agreement is found between measurements and calculations for distances above 30 nm, except for the symmetrical case with the emitter and the substrate both made of SiO_2 (Fig. A.3a). This disagreement may be explained by a frequency shift of the dielectric function observed by reflectivity measurements on the sphere compared to that of the bulk substrate, which may significantly affect radiative heat transfer (see section A.3). The sphere permittivity is therefore termed 'modified SiO_2'.

The largest near-field radiative conductance of 16.7 ± 3.3 $nW.K^{-1}$ is found for the modified SiO_2-graphite configuration (Fig. A.4c) with the sphere at 900 K, which is larger than the maximum value measured at 1200 K. This unexpected result is explained by the last distance before contact (driven by roughness and vibrations, see section A.4) that might be smaller for the experiment performed at 900 K, thus leading to a near-field radiative conductance larger than that measured at 1200 K.

For the modified SiO_2-InSb configuration (Fig. A.3b), both measurements and calculations level off at low distances because the dielectric functions of the two materials are not matching well in the frequency range where most of the radiative heat transfer occurs for temperatures ranging from 450 to 1200 K (see Fig. A.8a,b).

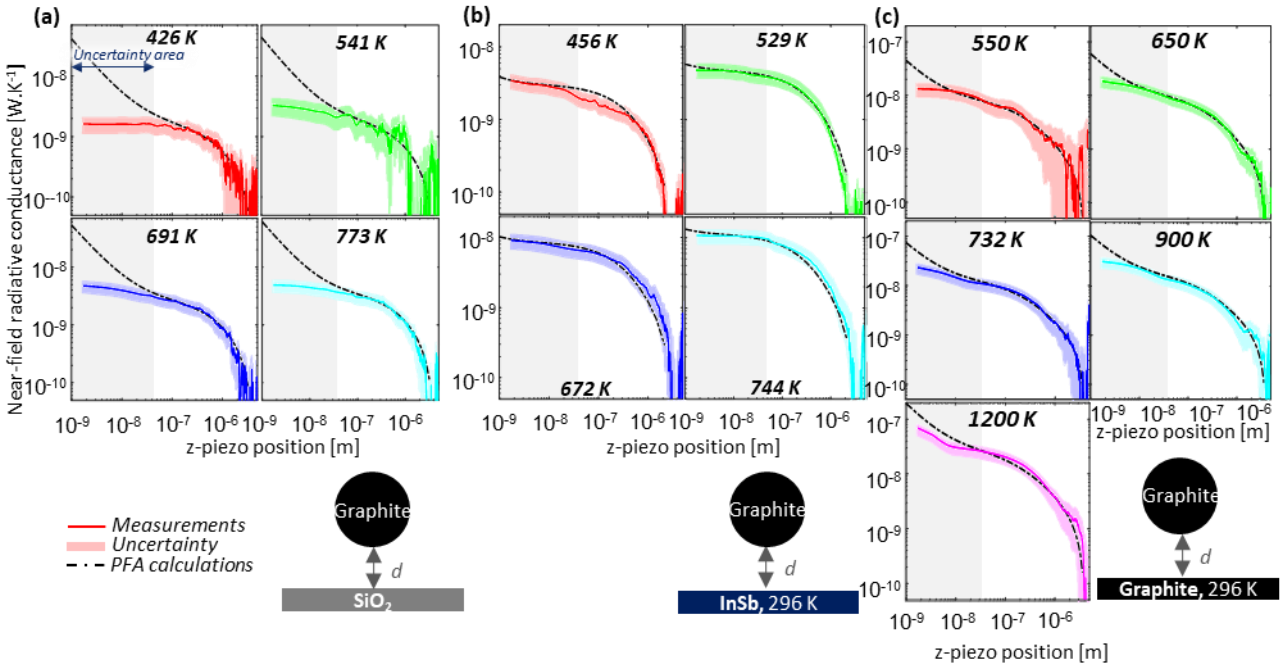

Fig. A.4: Near-field radiative conductance measurements with a graphite emitter. Near-field radiative conductance between a graphite sphere heated from 426 to 1200 K and a planar substrate at room temperature made of either SiO_2 (**a**), InSb (**b**) or graphite (**c**), as a function of z-piezo position. The grey-shaded area represents the range where there are large distance determination uncertainties induced by the roughness of the materials and mechanical vibrations.

If the SiO_2 sphere had the same permittivity as the substrate, the graphite-SiO_2 configuration (Fig. A.4a) would be the opposite in terms of materials compared to the SiO_2-graphite configuration previously studied. According to calculations, thermal rectification may be observed between the two configurations because of the temperature dependence of the dielectric function of SiO_2, which was measured in the work of Joulain *et al.*[1]. In this case, conductance differences up to a few percent may be expected. Unfortunately, the large distance uncertainties close to contact, the accuracy of the conductance measurement and the permittivity variation could not allow us to conclude on an observation of thermal rectification.

For the graphite-InSb configuration (Fig. A.4b) the temperature of the sphere is kept below the melting temperature of InSb because the thermal conductivity of graphite (25-470 $W.m.^{-1}K^{-1}$) is one to two orders of magnitude larger than that of SiO_2 (1.4 $W.m.^{-1}K^{-1}$). A contact between a graphite sphere heated above 800 K and an InSb substrate may damage the sample and pollute the sphere.

The symmetrical graphite-graphite configuration provides the largest conductance among all configurations studied in this work, with a maximum of 68.9 ± 13.7 $nW.K^{-1}$ measured at an emitter temperature of 1200 K (ΔT = 904 K).

A.3. Silica spheres

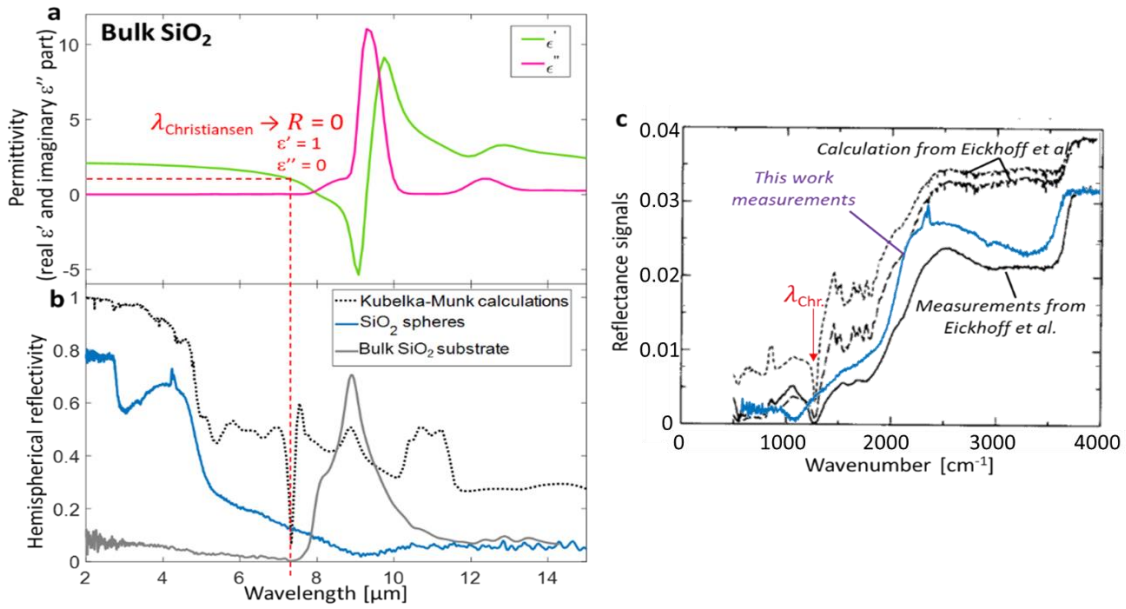

Fig. A.5: Reflectivity measurements on SiO_2 spheres compared to a bulk SiO_2 substrate. (**a**) Real and imaginary parts of the dielectric function of SiO_2 as a function of wavelength. The Christiansen wavelength where the reflectivity of the material is equal to 0 ($\boldsymbol{\varepsilon'} = 1$ and $\boldsymbol{\varepsilon''} = 0$) is highlighted. (**b**) Kubelka-Munk reflectivity calculations for the SiO_2 spheres compared to reflectivity measurements for the SiO_2 spheres and a bulk substrate. (**c**) Comparison of this work measurements with measurements and calculations from Eickhoff et al.[2].

The dielectric function of bulk SiO_2 measured by Joulain et al.[1] is shown in Fig. A.5a. SiO_2 has a Christiansen wavelength λ_{Chr}, where the refractive index of the material is the same as that of its environment (air in our case). Scattering nearly vanishes and almost all the light is transmitted if the material is not absorbing at λ_{Chr}, leading to a reflectivity that tends to 0. The zero-reflectivity value is measured at the expected wavelength for a bulk SiO_2 substrate (Fig. A.5b) and for the estimated reflectivity of the spheres calculated with the Kubelka-Munk theory[3]. However, λ_{Chr} seems to appear at a shifted wavelength for a sample made of SiO_2 spheres, meaning that their dielectric function is different from that of the bulk SiO_2. In Fig. A.5c, reflectivity measurements from this work are compared with similar measurements from the literature performed by Eickhoff et al.[2] with 4-40 µm in diameter SiO_2 spheres. The general behavior is similar between the two sets of measurements but that of Eickhoff exhibits a zero-reflectivity measurement at the expected Christiansen wavelength, contrary to the measurements of this work where λ_{Chr} appears again with a shift. The comparison of λ_{Chr} between a bulk SiO_2 substrate, the spheres used during this work and measurements from literature, allows to conclude that the dielectric function of this work's SiO_2 spheres is different from that of the bulk substrate and may explain the disagreement between the near-field radiative heat transfer measurements and calculations for the symmetrical SiO_2-SiO_2 case.

For this configuration, surface phonon polaritons (SPhPs) supported by the sphere and the substrate are expected to have the same frequency, thus enhancing drastically radiative heat transfer in the near field. A frequency shift of the dielectric function for the sphere may lead to a non-matching of the SPhPs frequencies between the emitter and the substrate. For configurations with a substrate made of another material than SiO_2, no match of SPhPs frequencies is expected, so that a dielectric function

of the SiO_2 sphere slightly different than expected should not have any significant impact on near-field radiative heat transfer.

A.4. Distance determination

(a)

Sample	RMS roughness (nm)		Minimum (nm)	Maximum (nm)	Mean spacing of irregularities (µm)
SiO_2 bulk	1.1	1.3	-4.1	5.0	2.57
InSb bulk	0.1	0.2	-0.7	0.8	4.91
SiO_2 sphere	2.6	3.4	-19.9	15.8	0.05
Graphite sphere	5.2	6	-28.7	29.9	0.03

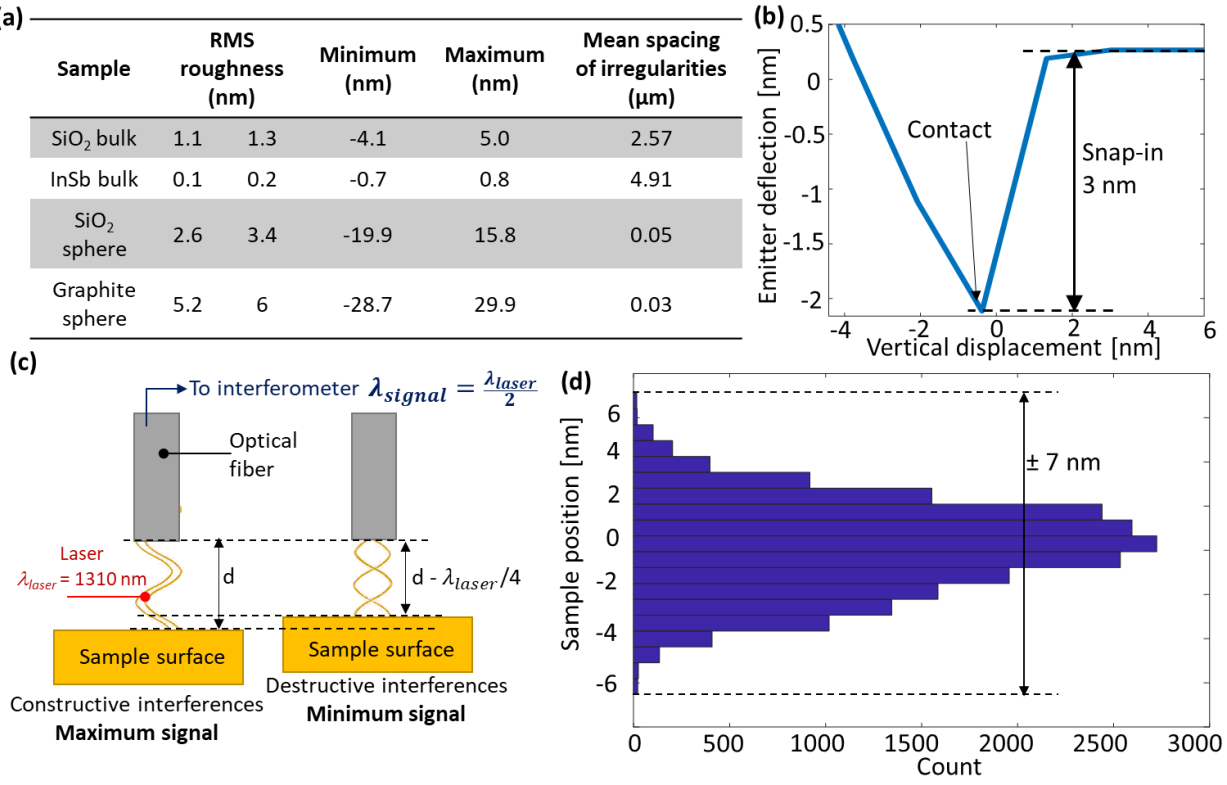

Fig. A.6: Determination of the distance uncertainty close to contact. (a) Roughness measurements performed with atomic force microscopy (AFM) on bulk samples and on the SiO_2 and graphite spheres. (b) Emitter deflection measurement as a function of its vertical displacement measured with an AFM setup. (c) Interferometric measurement setup of the mechanical vibrations of the sample. The fiber is placed at an intermediary position between a maximum and a minimum of the interferometric signal where the amplitude of the signal depends linearly on the distance d. (d) Histogram of the position of the sample around its mean position, measured with the interferometric setup.

The distance uncertainty at which the contact between the spherical emitter and the substrate occurs was estimated based on roughness, mechanical vibration and snap-in measurements. The roughness of bulk samples and spheres was measured by atomic force microscopy (AFM). The table in Fig. A.6a summarizes the root-mean-square (RMS) roughness measured on two different sets of samples for each case, the minimum and maximum height of irregularities, and the mean spacing between irregularities. The bulk substrates are very flat with irregularities having a maximum height of a few nanometers. However, the roughness of the spheres is more important with irregularity heights up to 30 nm and more closely spaced compared to those of bulk substrates.

The snap-in of the emitter close to contact was also measured using an AFM setup. Here a laser beam illuminates the cantilever of the SThM probe (where the sphere is attached) and the reflected beam is collected by a quadrant photodiode. When the cantilever bends, a deflection signal is measured and assumed to be proportional to the amplitude of the bending. Close to contact, attraction forces between the spherical emitter and the substrate can bend the cantilever and bring the sphere into

contact with the substrate (snap-in). In Fig. A.6b, a snap-in distance of 3 nm is measured, and thus contributes very little to the distance uncertainty compared with the roughness of the spheres.
Vibrations of the setup were measured using an interferometric unit with an optical fiber (Fig. A.6b) by illuminating the surface of the sample with a laser beam having a wavelength of 1310 nm. The laser beam is reflected on the sample and collected back by the fiber and sent to the interferometric unit. The resulting signal, having a wavelength equal to half that of the laser, is used to determine the oscillations of the sample around its mean position. A histogram of the positions of the sample is provided in Fig. A.6c. It appears that the sample oscillates around its mean position with an amplitude of 7 nm.
Adding the contributions of the roughness, the snap-in and that of the vibrations leads to a distance uncertainty of 30 to 40 nm depending on the material of the sphere (the graphite spheres have a larger roughness than modified silica ones).
Thermally-induced deflection of the SThM probe to which the emitter is glued was investigated in order to estimate its effect on distance uncertainty. Fig. A.7a shows the vertical deflection, measured using an AFM setup, of three different {sphere+cantilever} systems as a function of their temperature in absence of piezoactuator displacement. It indicates that increasing the temperature bends the SThM probe upwards (positive values) most of the time but can also bend the probe downwards (negative values, in the case of emitter 3). Large deflection differences found between the three cantilevers suggest that the thermally-induced deflection is strongly cantilever-dependent. In the worst case (emitter 1), a deflection of about 2 $nm.K^{-1}$ is observed, which indicates that temperature variation during an approach curve should not lead to significant deflection. Furthermore, we measured the vertical deflection at different emitter temperatures under low vacuum during an approach-withdrawal process over a 300 nm distance range (Fig. A.7.b). We did not observe any influence of the emitter temperature on the snap-in distance close to contact, meaning that it is mostly due to attraction forces and not due to vertical deflection related to a temperature change of the emitter caused by near-field thermal radiation. Finally, Fig. A.7c shows the temperature variation of a graphite emitter set at 900 K and a graphite substrate at room temperature (300 K) during an approach where near-field thermal radiation occurs. It highlights that the temperature difference between the largest and smallest sphere-substrate distance is only around 0.6 K, which confirms the negligible change in the vertical deflection anticipated from Fig. A.7a

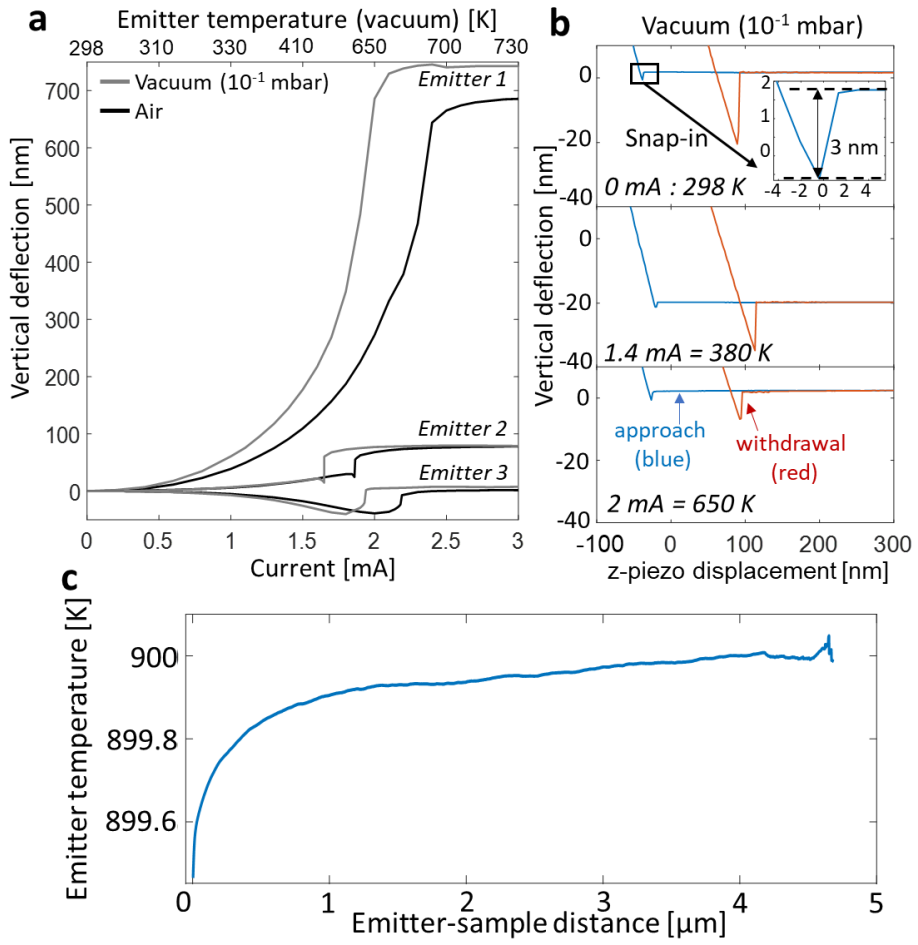

Fig. A.7: Influence on the distance determination of the temperature-induced vertical deflection of the probe. (a) Measurements of the vertical deflection as a function of electrical current and temperature of three different emitters using an AFM setup in air and under low vacuum. (b) Vertical deflection of an emitter as a function of z-piezo displacement, measured during the approach, contact with a sample and withdrawal for different emitter temperatures. (c) Temperature drop due to near-field thermal radiation between a graphite emitter heated at 900 K approaching a graphite sample at 300 K.

An estimation of the minimum distance d_{min} reached during the radiative heat transfer experiments can be made by applying a distance shift to the measurements in order to best fit to the PA calculations. To obtain the value of d_{min}, a series of distance shifts is applied to each measurement in order to minimize the root-mean-square error between the measured and the calculated distances below 300 nm. The shifted measurements and PA calculations are represented in Fig. A.8 for each pair of materials. Except for the SiO_2-SiO_2 case (see section A.3), a good agreement is found between the shifted measurements and calculations. The average estimated d_{min} are listed in each sub-figure and are ranging from 6 up to 56 nm (excluding the SiO_2-SiO_2 case), which is an agreement with the distance uncertainty range that was found with the roughness, snap-in and vibration analysis.

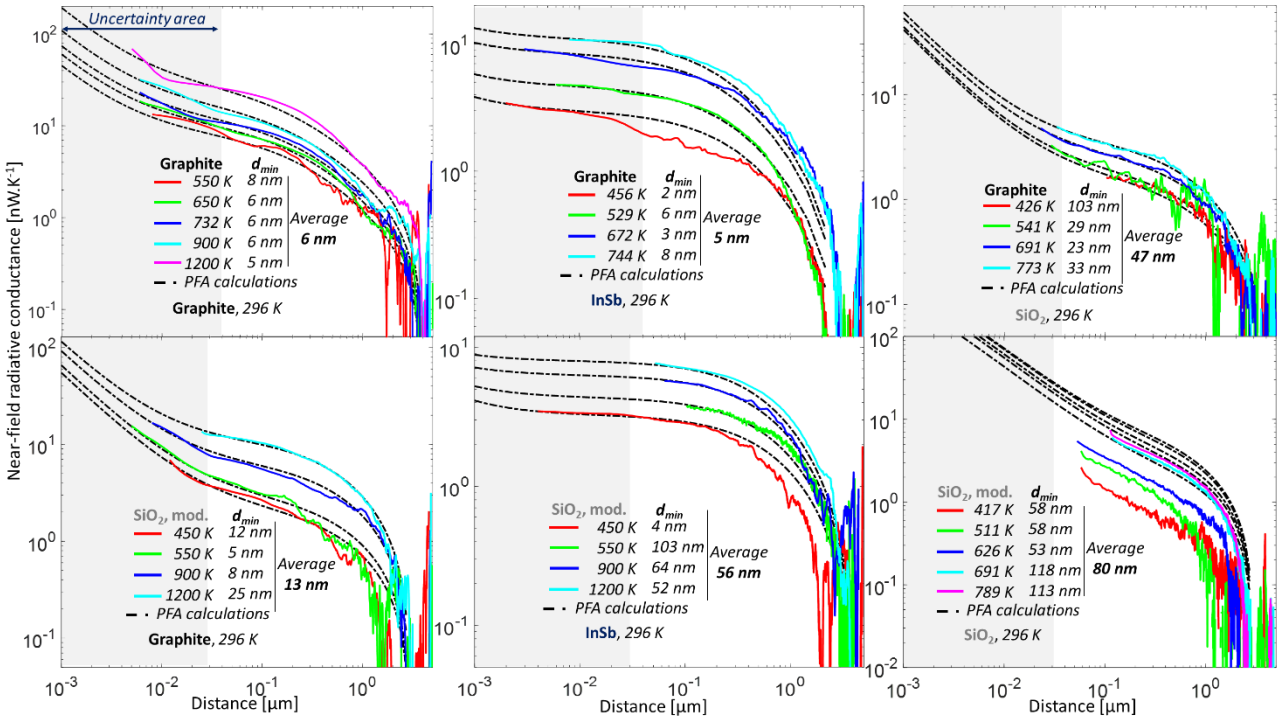

Fig. A.8: Experimental estimation of the minimum distance before contact. Near-field radiative conductance calculations using PFA are compared with measurements after fitting and adjusting the distance scale.

A.5. Dielectric functions

This section provides the real and imaginary parts of the dielectric functions of each material. Data for SiO_2 and graphite come from measurements performed respectively by Joulain et al.[1] (from room temperature up to 1480 K, measurements at 295 K are represented in Fig. A.9a) and Querry[4] (data at room temperature only). In the case of InSb the dielectric function was calculated by Vaillon et al.[5].

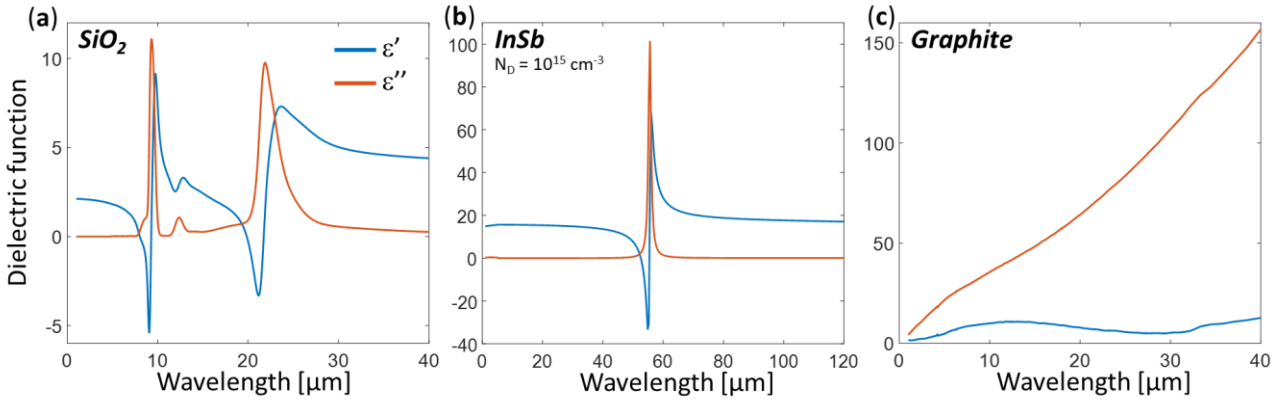

Fig. A.9: Dielectric function at room temperature as a function of wavelength for the different materials. (**a**) SiO_2 from Joulain et al.[1], (**b**) InSb from Vaillon et al.[5] and (**c**) graphite from Querry[4].

A.6. Near-field radiative heat transfer calculations for the plane-plane configuration

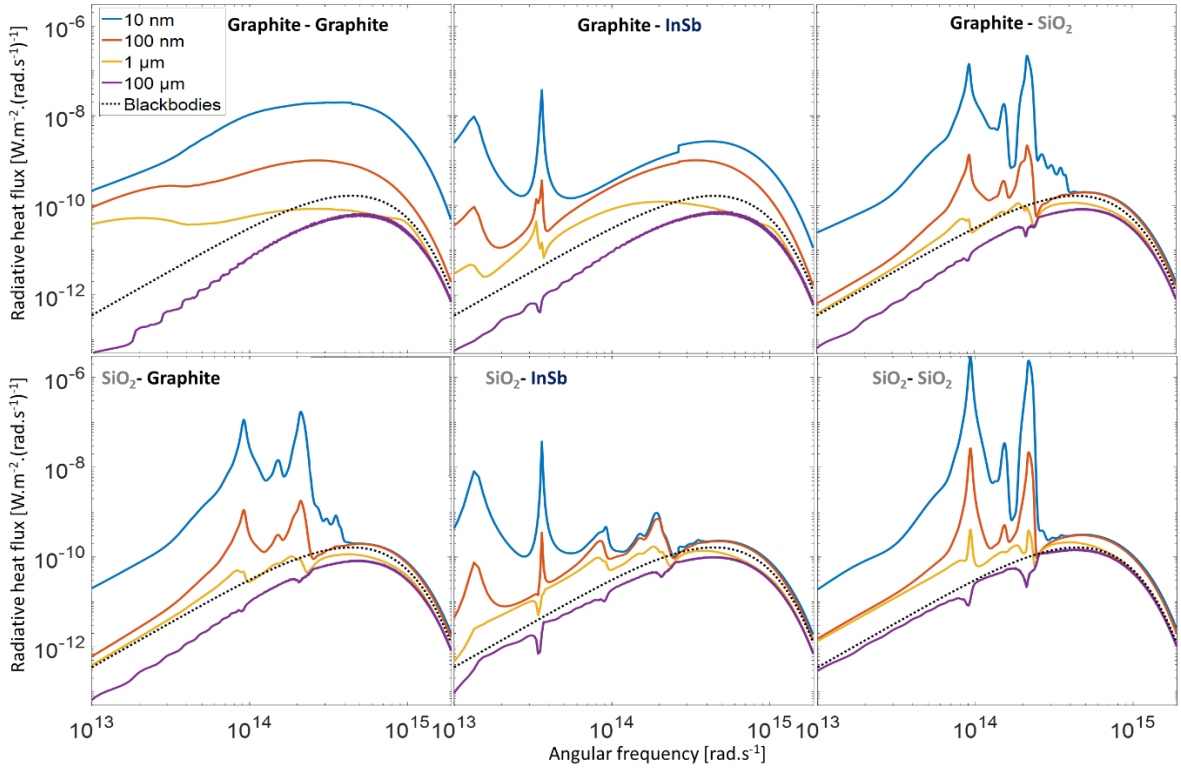

Fig. A.10: Radiative heat flux as a function of angular frequency between planar bodies at 1200 K, made of graphite or SiO_2, and planar bodies at 300 K made of either graphite, InSb or SiO_2.

Fig. A.10 represents the radiative heat flux between a planar body made of graphite or SiO_2 at 1200 K and planar bodies at 300 K made either of graphite, InSb or SiO_2. The figure shows the spectra calculated at distances of 100 µm, 1 µm, 100 nm and 10 nm compared to the radiative flux exchanged between two blackbodies. The radiative flux is mainly enhanced at low frequencies but with peaks appearing at the resonance frequencies of the surface polaritons of SiO_2 and InSb. In the far field the fitted flux using the temperature power law (Eq. 3 in the main text) leads to an exponent n_{FF} exceeding the value of 4 (see Fig. 4) representative of the blackbody. This is due to the shape of the spectra of the radiative heat flux for these materials in the far field (curve at d = 100 µm in Fig. A.10). These spectra are lower in amplitude than that between two blackbodies with larger differences at low frequencies meaning a lower emissivity, well seen for the SiO_2-graphite configuration. When temperature increases, the frequency of the maximum radiative heat flux ω_{Wien} is shifted towards high frequencies (from 1.1 10^{14} at 300 K to 4.4 10^{14} at 1200 K), where the shape of the spectra for the real materials are close to that of the blackbodies. Therefore, the radiative heat flux in the far field for these materials is enhanced at a faster apparent rate than that between two blackbodies, because of the increasing emissivity of the material at high frequencies.

A.7. Calibration of the emitter

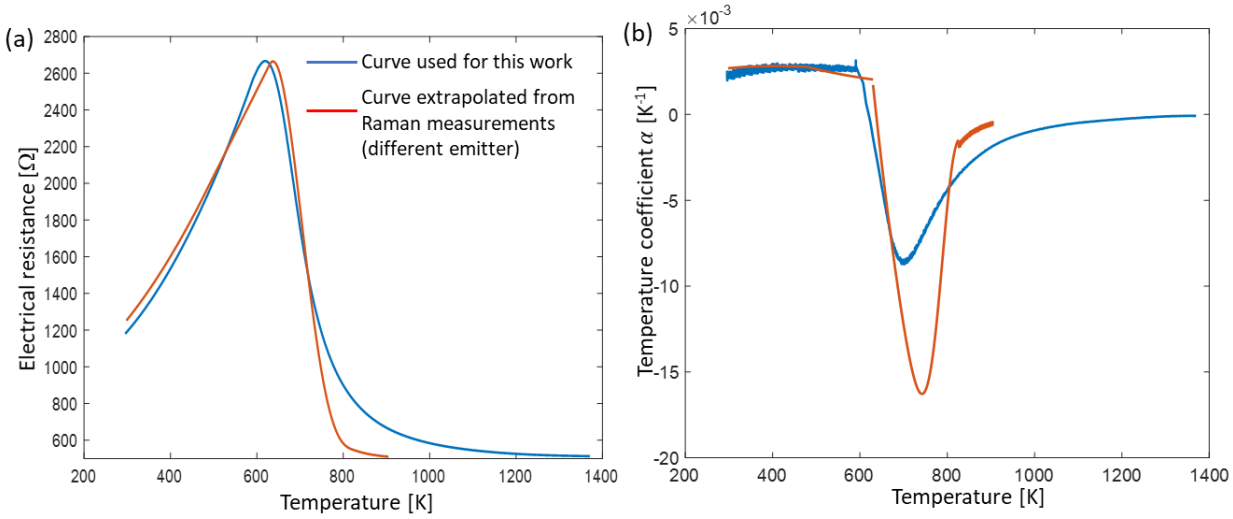

Fig. A.11: Comparison of two emitter calibration methods. (a) Electrical resistance as a function of temperature. The blue curve shows the calibration curve used for this work and obtained using the method described in section A.2. The red curve corresponds to a calibration curve extrapolated from Raman temperature measurements performed on another emitter. (b) Temperature coefficients calculated from the two calibration curves.

In order to verify the accuracy of the calibration method described in section A.2, Raman temperature measurements were performed on an emitter while heating it with an electrical current and measuring its electrical resistance at the same time (Fig. A.11a). It is important to remark that the two curves correspond to two different emitters that may have significantly different behaviors, as they are based on SThM probes whose properties strongly depends on fabrication process parameters (doping level). The two curves are very similar up to 750 K but deviate strongly at higher temperatures up to a relative difference of 25 % at 1200 K. This difference is slightly higher than the uncertainty of 20 % considered in this work. Concerning the temperature coefficient α (Fig. A.11b), differences up to a factor of 2 are observed between the two curves. However, possible errors on α have a limited impact on the calculation of the near-field radiative thermal conductance (Eq. 2 in the main text) because in the equation, α is multiplied by a term (temperature difference) that depends on the inverse of α. Considering the calibration curve extrapolated from Raman measurements, calculations of near-field radiative conductance and exponent of the temperature power law respectively led to differences of 10 and 15 % respectively.

To summarize, emitter temperatures larger than 750 K that have been measured during this work could have been overestimated by a factor up to 25 % (reached at 1200 K), leading to a conductance overestimated by up to 10 % and an exponent underestimated by up to 15 %. Except for measurements at 1200 K, these potential errors on temperature, conductance and exponent are smaller than the 20 % uncertainty already considered. Near-field radiative heat transfer experiments using Raman-calibrated emitters may help in order to improve the accuracy of the measurements in the future[6].

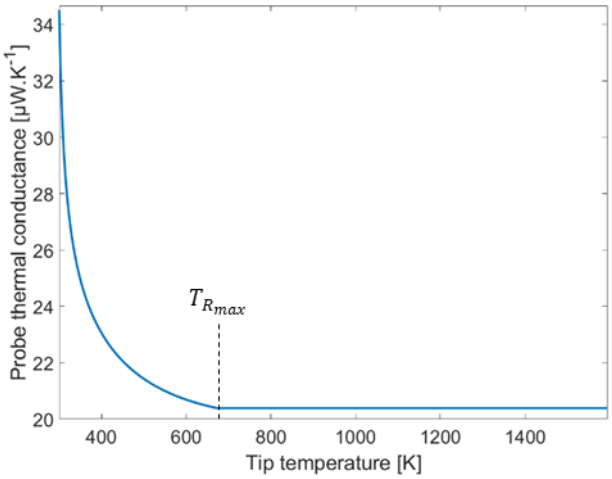

Fig. A.12: Probe thermal conductance as a function of tip temperature measured under vacuum with a surrounding temperature of 300 K.

The probe thermal conductance shown in Fig. A.12 accounts for heat conduction through the cantilevers (support beams) of the SThM probe. The thermal conductance G was measured under vacuum at a room temperature T_{amb} = 300 K by gradually increasing the electrical power supplied to the probe while measuring its electrical resistance and determining the tip temperature T. Then the thermal conductance of the probe was calculated as $G = \frac{P}{T - T_{amb}}$. As the tip temperature increases, thermal conductance decreases until it reaches a stable value around 20.5 µW.K^{-1} for temperatures higher than the temperature of maximum electrical resistance T_{Rmax} (see Fig. A.11 and Fig. 1). In this range, the thermal conductance of the probe is constant because the temperature is proportional to the electrical power as discussed by Spieser *et al.*[7].

A.8. Uncertainty on the exponent of the temperature power law

The experimental measurements of radiative flux (or conductance) are fitted using Eq. (3) of the main text for each distance and for a large set of pre-factors C and exponents n. The best fit is found when the root-mean-square difference between the fitted and experimental fluxes is minimum. Fig. A.13 shows the data for the SiO_2-InSb case at a distance of 1 µm. In this case, fitting the experimental data leads to an exponent of 2.92 for the best fit, to be compared with 2.31 which is expected theoretically using the proximity approximation. The uncertainty for the exponent n is determined by finding the maximum and minimum values of n allowing the fit to be included in all experimental error bars, either considering only the uncertainty on the conductance G or the uncertainty on both G and the emitter temperature T. In Fig. A.13 the fit with the maximum exponent n considering the uncertainty on G or both on G and T (respectively equal to 3.59 and 4.66) is plotted in red (solid and dash-dotted lines) and that with the minimum exponent (respectively equal to 2.08 and 1.55) is plotted in purple (solid and dash-dotted lines). The points where the fitted curves cross the limits of the error bars are highlighted by green and dark-blue dots, considering respectively the uncertainty on G or both on G and T. For instance, it appears clearly with a logarithmic scale (Fig. A.13b) that the maximum exponent is limited by the uncertainty of the second and last experimental point, and by the first and last point for the minimum exponent.

Considering both uncertainties on G and T instead of only that on G leads to a significantly larger uncertainty on the exponent. This effect is even bigger when the emitter temperature range in which the experiments were performed is reduced (see Fig. 4 in the main text). For instance, emitter temperatures for the SiO_2-InSb case represented in Fig. A.13 are ranging from 450 to 1200 K, while the graphite-InSb case is limited to a 456-744 K range. Here, the uncertainties on G and T are considered uncorrelated, leading to rectangular uncertainty zones in Fig. A.13 (light blue zone, $\pm\Delta T, \pm\Delta G$). In reality, these uncertainties are correlated since they are both due to the uncertainty on temperature calibration. The rectangle shape therefore clearly overestimates the uncertainty zone. In Fig. 4 of the main text, we provide both the underestimated (only G, dark grey) and overestimated (both G and T, light grey) uncertainties, while we remind only the first one in Tab. 1 for practical reasons (asymmetric $\pm\Delta n$ for (G, T) case as seen in Fig. 3).

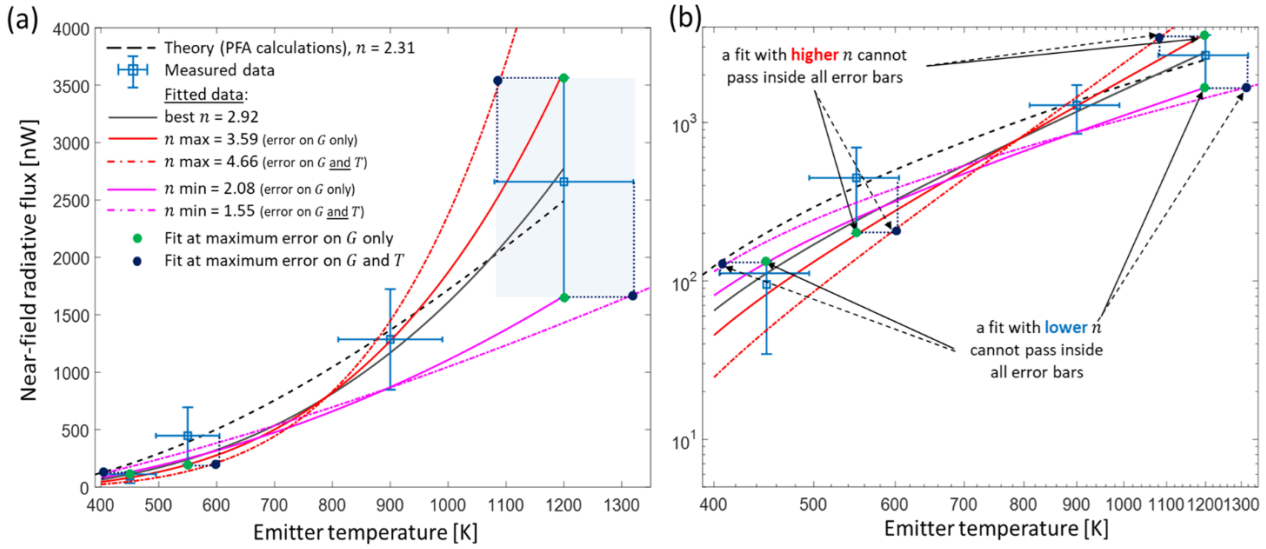

Fig. A.13: Determination of the exponent of the temperature power law. (a) Near-field radiative flux as a function of emitter temperature between a SiO_2 sphere and an InSb substrate separated by a distance of 1 μm. Squares with error bars are measured data with uncertainties, the dotted curve is the expected flux predicted by the proximity approximation, the grey curve is the best fit and the red and purple curves (both solid and dash-dotted curves) are fits allowing respectively the maximum and minimum exponent n while passing inside all error bars considering either only the uncertainty on the conductance G (solid curves) or both uncertainties on G and emitter temperature T considered as uncorrelated. (dash-dotted curves) (b) Same data as (a) but in logarithmic scale.

References

1. Joulain, K., Ezzahri, Y., Drevillon, J., Rousseau, B. & De Sousa Meneses, D. Radiative thermal rectification between SiC and SiO_2. *Opt. Express* **23**, A1388 (2015).
2. Eickhoff, T., Grosse, P. & Theiss, W. Diffuse reflectance spectroscopy of powders. *Vib. Spectrosc.* **1**, 229–233 (1990).
3. Kubelka, P. & Munk, F. Ein Beitrag Zur Optik Der Farbanstriche. *Z. Für Tech. Phys.* **12**, 593–601 (1931).
4. Querry, M. R. Optical constants. *Contract. Rep. Sep 1982 - May 1984 Mo. Univ Kans. City* (1985).
5. Vaillon, R. *et al.* Micron-sized liquid nitrogen-cooled indium antimonide photovoltaic cell for near-field thermophotovoltaics. *Opt. Express* **27**, A11 (2019).
6. Piqueras, M. *et al.* Temperature calibration of doped silicon based scanning thermal microscopy. *Submitted* (2021).